JTTEE5 6:57-66

Mechanical Properties Testing and Results for Thermal Barrier Coatings

T.A. Cruse, B.P. Johnsen, and A. Nagy

Mechanical test data for thermal barrier coatings, including modulus, static strength, and fatigue strength data, are reviewed in support of the development of durability models for heat engine applications. The materials include 7 and 8 wt% yttria partially stabilized zirconia (PSZ) as well as a cermet material (PSZ + 10 wt% NiCoCrAlY). Both air plasma sprayed and electron beam physical vapor deposited coatings were tested. The data indicate the basic trends in the mechanical properties of the coatings over a wide range of isothermal conditions. Some of the trends are correlated with material density.

Keywords coatings, durability, isothermal, properties, thermal barrier

1. Introduction

1.1 *Background*

THE GOAL in mechanical characterization of thermal barrier coating (TBC) systems is to provide sufficient data on material behavior for life prediction of the systems under complex thermomechanical loading environments in heat engines. This goal differs in thrust and approach from what might be called material screening tests, which seek to rank-order material durability under a specified test environment. Thus, we seek to characterize the stress-strain-temperature behavior of the TBC systems under conditions that are well enough controlled that specimen geometry or loading condition influences are minimized. The operating hypothesis is that we can develop empirical models for correlating fatigue life of the TBC systems under cyclic thermomechanical conditions if we have sufficient mechanical property characterization under ideal conditions. Thus, the testing requirements fall between material screening and engine testing.

The mechanical properties of interest include modulus, strength, creep rate, and fatigue strength . However, experience has shown that cyclic properties, rate effects, in situ residual stresses, and orientation of the TBC material are important to correlating thermomechanical life data.

1.2 *Life Modeling*

Fatigue life prediction models have been proposed by the principal author of this report for two coating methods in gas turbine engine applications (Ref 1, 2). A third model for high-cycle fatigue conditions in diesel engine applications is discussed in this paper. Life prediction for turbine engine applications focused on the cyclic thermomechanical strain conditions experienced by critical locations on coated turbine blades and vanes. Diesel engine applications considered isothermal fatigue test conditions. Mechanical testing in these programs therefore considered a wide range of temperature conditions and strain cycles in both tension and compression.

The first turbine engine life model was proposed for an air plasma sprayed 7 wt% yttria PSZ material (Ref 3). The life modeling was based on the observation of cyclic thermomechanical fatigue microcrack generation and extension. Cyclic hysteresis in the TBC under thermomechanical conditions was modeled using a state variable model of the thermoviscoplastic material. Parameters for the material model were taken from the uniaxial test results that were reported in Ref 1. The testing methodology and results are referred to in this paper as Phase 1 tests (plasma-sprayed PSZ for turbine engines).

The second life prediction model was for the same material but deposited by an electron beam physical vapor deposition (EB-PVD) process, as reported in Ref 2. More details of the material conditions are given in Ref 4. In this case, the PSZ has a columnar structure that is quite resistant to cracking parallel to the bond coat interface. The mechanical test results indicated that the EB-PVD material had substantially higher strain levels of elastic behavior than the air plasma sprayed ceramic coating.

Thermomechanical fatigue failures of the TBC occurred within the oxide layer buildup on the bond coat. The best life correlations were achieved by a fatigue model of the oxide layer in the bond coat itself (Ref 2, 4). In order to make these predictions, the elastic properties of alumina were used to model the thermally grown oxide on the bond coat. The testing methodology and results are discussed in this paper as Phase 2 tests (EB-PVD coating for turbine engines).

The testing of TBC materials reported in this paper seeks to provide insight into the high-cycle fatigue behavior of ceramic coatings for diesel engine application. The diesel application is characterized by compressive surface stress cycles superimposed on a steady compressive stress background and is associated with the effect of the individual cylinder combustion cycles superimposed on a steady-state engine power condition. Spallation of the TBC was observed to progress from the outer surface, growing over time, and is illustrated in a fatigue specimen failure mode in Ref 5. Mechanical testing in this program therefore concentrated on isothermal fatigue and compressive strength testing at room temperature and temperature levels experienced under steady-state engine operation.

The diesel engine high-cycle fatigue life prediction model requires basic thermoelastic properties for the TBC, together with compressive fatigue testing at various levels of compressive

Thomas A. Cruse and **B.P. Johnsen,** Vanderbilt University, Nashville, TN 37235, USA; and **A. Nagy,** Southwest Research Institute, San Antonio, TX 78228, USA.

stress cycling and stress ratios, R ($R = \sigma_{max}/\sigma_{min}$). The Phase 1 tensile fatigue testing on plasma-sprayed 7 wt% yttria PSZ resulted in isothermal fatigue strengths approaching the ultimate strength of the material (Ref 6,7). Further isothermal fatigue test results, life modeling, and physical interpretations of the fatigue failures are given in this paper. The testing methodology and results are discussed in this paper as Phase 3 tests (plasma-sprayed PSZ and cermet materials for diesel engines).

2. Specimen Selection and Tests

2.1 *Phase 1 Mechanical Tests—Air Plasma Sprayed TBC*

The various test methods reported in this section are all nonstandard tests. The reasons for the use of nonstandard tests are: (a) the limited thickness of the TBC material as deposited by standard coating processes; (b) the deposition process itself, which requires the use of a substrate material for solidification or deposition; (c) the unique mechanical characteristics of the various TBC materials, with their inherent lack of significant tensile strength, and (d) the need to achieve stress states that are uniform tension or compression for the entire specimen cross section.

The Phase 1 and 2 test programs required both tensile and compressive load tests. All testing was performed isothermally at a range of test temperatures from room temperature to 1300 °C. All specimens were designed so that the primary (or only) applied stress was oriented parallel to the coating-substrate interface. In the case of the plasma-sprayed materials, the loading was parallel to the splat structure of the coating; in the case of the EB-PVD material, the loading was transverse to the columnar growth structure of the coating.

Phase 1 tensile testing used a "bowtie" tensile bar and the "Brazil" wafer specimen, which has the appearance of a large aspirin tablet. Both specimens were machined from TBC that was deposited on a flat surface and had rectangular cross sections (Ref 3). The two specimens are shown in Fig. 1. The test apparatus was a standard computer-controlled test machine. In the case of the tension test, a highly flexible load train was used to minimize bending strains on the specimen. The wafer test is performed in compression by placing the specimen between two anvils; the normal stress on a plane connecting the load points is a nearly uniform tensile stress (Ref 8).

The bowtie tensile specimen was analyzed to determine the stress concentration factor at the end of the gage section, because the lower temperature tests failed at this location. The stress concentration factor was found by stress analysis to be 1.15. That value resulted in similar tensile strengths for the two specimens. The two sets of tensile strength data are reported in the next section. The major problem in both specimens was the inability to provide axial strain measures to be used in making accurate modulus measurements. The bowtie tensile test strains were calculated by a room-temperature calibration test of a strain-gaged specimen; the elevated-temperature testing was assumed to have the same load system flexibility. The digitized strain data were then subtracted from the load system deflections in order to obtain stress-strain curves for each tensile test. Stress-strain curves are reported for these tests in Ref 3.

The bowtie specimen was also used for tensile creep strain rate data at the higher test temperatures. The specimen failures shifted to the gage section in the creep tests, showing that the material lost its notch sensitivity under these conditions.

The lack of good strain measures is a continuing problem for many of the reported tests. Extensometers are generally too heavy for testing unsupported TBC coating specimens. Laser strain measurement methods would alleviate the problem but at significant increases in test cost and setup time.

The Phase 1 compression testing used solid cylindrical specimens that were ground from the thick TBC that had been previously deposited on a substrate. The specimens were 3.12 mm in diameter and 6.35 mm long. Again, the test direction was aligned parallel to the splats. The specimens were compressively loaded between two anvils (Ref 3).

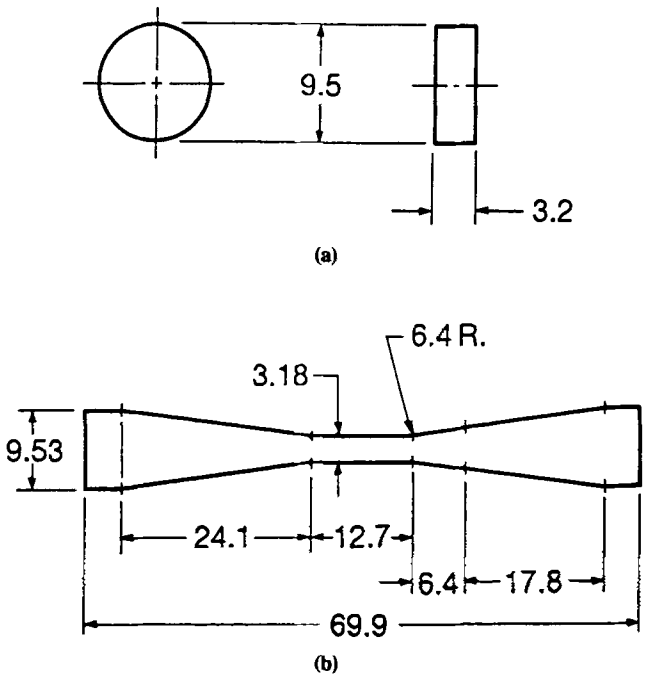

Fig. 1 Rectangular-section tension specimens used for Phase 1 testing. (a) Wafer specimen. Wafer is tested in compression on a diametral axis but produces tension on the section perpendicular to the compression axis. (b) Bowtie specimen. Dimensions are given in millimeters.

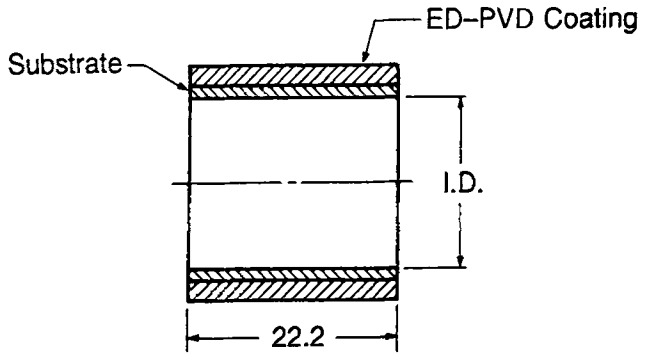

Fig. 2 Composite compression specimen used in Phase 2 testing, with the TBC deposited on PWA 1480 substrate. Dimensions are given in millimeters.

The compression testing was generally successful in that the failures appeared to originate in the central regions of the test specimen and not near the ends. High-temperature lubricant was used to minimize end restraint during the compression testing. The alignment was approximately 0.02% on the diameter. Alignment was achieved using shims and was confirmed by a strain-gaged metallic test bar.

The compression stress-strain curve data were obtained by running each test temperature to the full ceramic specimen loads, but with no specimen between the anvils. The digitized load-deflection curves were stored for each temperature and then were subtracted from the appropriate test data of load system deflection versus load.

2.2 *Phase 2 Mechanical Tests—EB-PVD Thermal Barrier Coating*

Phase 2 testing was performed on EB-PVD thermal barrier coating material. The material was deposited on single-crystal nickel superalloy tubes and was assumed to have negligible tensile strength. Therefore, the TBC/metal system was tested as a composite system. The metal bar dimensions were selected with different strategies for tension and compression. In the case of the compression test specimen in Fig. 2, the tube geometry was selected to meet the following estimated constraints: (a) wall buckling of the metal tube defined a relation between the thickness and radius of the metal substrate; (b) wall thickness of the metal substrate was set to ensure that the TBC section stiffness was comparable to or greater than that of the substrate section; and (c) wall thickness of the TBC was as great as production would permit.

The compression specimen thickness was selected on the basis of the plasma-sprayed TBC compression modulus. The substrate inner diameter was ~18 mm, the specimen length was ~22 mm, and the substrate wall thickness was ~2.2 mm. Compressive axial strains were measured by an Instron capacitive strain transducer.

In the case of tension testing, the TBC was again deposited on a superalloy tube of PWA 1480 single-crystal material. However, the tube inner surface was then machined to a wall thickness of about 0.36 mm with a TBC thickness of about 4.6 mm. The specimen substrate cross section was reduced in the region of the TBC. TBC adherence to the ends of the substrate gage-reduction zone was desired in order to minimize intermaterial shear as the loading mechanism. The entire test specimen was sized for the use of an internal extensometer and is shown in Fig. 3.

The axial strains were measured by an internally mounted biaxial extensometer. The extensometer measured the axial strains over the length of the coating on the tubular specimen. Attempts were made to correlate the internal strain measure on the substrate to axial strains on the TBC coating by applying foil-type strain gages to the EB-PVD coating. However, failure of the adhesive caused this approach to be abandoned. A second extensometer was developed for external attachment in a room-temperature test. The external clip gage measured coating strains, which were about a factor of 2 lower than those measured internally after a strain of about 0.5%.

The strain data for the composite specimens were obtained by developing a composite load-deflection model for the material system of the TBC and the substrate. The compression specimens exhibited elastic/perfectly plastic behavior in the substrate. Some of the single-crystal substrates showed that a single slip system was active at high loads, resulting in a very nonuniform strain of the TBC. The elastic-plastic properties were measured in tests of the substrate material. Poisson's ratios were assumed but were found not to have a major effect on the stress-strain algorithm that was reported in Ref 9. An algorithm for subtracting out the TBC stress-strain response from the load-displacement curve is given in the same reference.

The tensile test behavior was quite different in that the TBC had very limited tensile ductility. The substrate, on the other hand, remained elastic at the appropriate load levels. The analysis was usable only to the point of significant damage to the ceramic coating. However, as discussed below, the tension tests did offer good insight into the tensile behavior of the EB-PVD ceramic coating.

2.3 *Phase 3 Mechanical Tests—High Cycle Fatigue of Air Plasma Sprayed TBC Material*

Phase 3 testing has been reported in Ref 7 and will only be summarized here. All of the testing in Phase 3 was in compression, with the specimen shown in Fig. 4. The primary focus of the testing was to establish the isothermal fatigue strength of the plasma-sprayed TBCs under pure compression loading. However, the testing produced some data of compressive strength, modulus, and cyclic stress-strain behavior.

The compression testing used two cylindrical test geometries. Both geometries were fabricated initially by spraying the TBC on iron substrates, then removing the substrates by acid etch. The compression loading was again parallel to the splat structures of the materials. Specimen alignment was critical because the Phase 3 specimens were much bigger than the compressive specimens in Phase 1 and lacked the metal substrate used in Phase 2.

The modulus measurements in the Phase 3 testing were made from load-deflection data. The digitized data were obtained from sampling at several ranges, and these curves were used to obtain modulus data.

3. Modulus and Strength Results

The Phase 1 test program showed that the tensile behavior of the plasma-sprayed TBC material is nonlinear over the entire

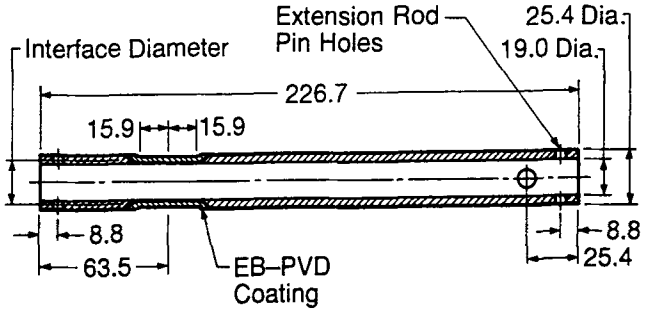

Fig. 3 Composite tensile specimen used in Phase 2 testing, with the TBC deposited on PWA 1480 substrate. Interface diameter was approximately 20 mm. Dimensions are given in millimeters.

range of strain to failure (Ref 3). The nonlinear behavior may be attributed to the generation and extension of a distributed network of microcracks inherent to this system. The Phase 2 tension testing indicated somewhat more linear behavior up to about 0.04% strain, followed by nonlinear behavior to fracture (Ref 4). The change in behavior at 0.04% strain is indicative of a residual stress effect, because the material is probably going from initial compression to tension. Compression testing, on the other hand, showed results that had distinctly linear portions up to temperatures around 1200 °C. This indicates that compression loading of the TBC material is not generating and extending the microcracks to the extent that the specimen compliance is affected for these applied stresses.

The modulus data versus test temperatures (Fig. 5) for all three test phases include both tension (initial slope) and compression data from Phase 1 and Phase 2, while all Phase 3 data were compressive (Table 1). For reference, the beam bending data of Brink (Ref 5) indicate a modulus value of 44 GPa for a 7.5 wt% yttria PSZ at 400 °C.

There were two populations of data: more tensile data in the upper population and more compressive data in the lower population, especially at the higher temperatures. The tensile data were associated with strains less than 0.1 to 0.2%, while the compressive data were taken with strains generally exceeding 1%. The tensile moduli were generally taken as initial slopes to the (strain softening) stress-strain curves and were more subject to error. The bulk compressive specimens for the range of TBC materials tested yielded reasonably consistent modulus results. These results show that the compressive moduli are below those of the tensile data and the reported data for flexure specimens. Further, the modulus values decreased in a steady manner be-

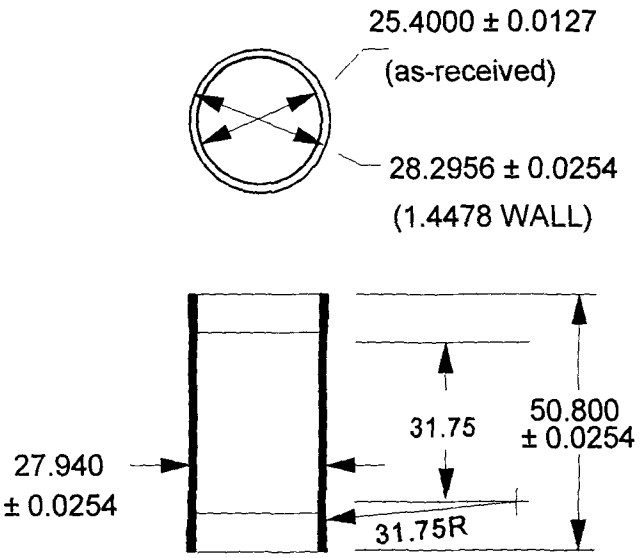

Fig. 4 Compression strength and fatigue specimen used in Phase 3 testing. Dimensions are given in millimeters.

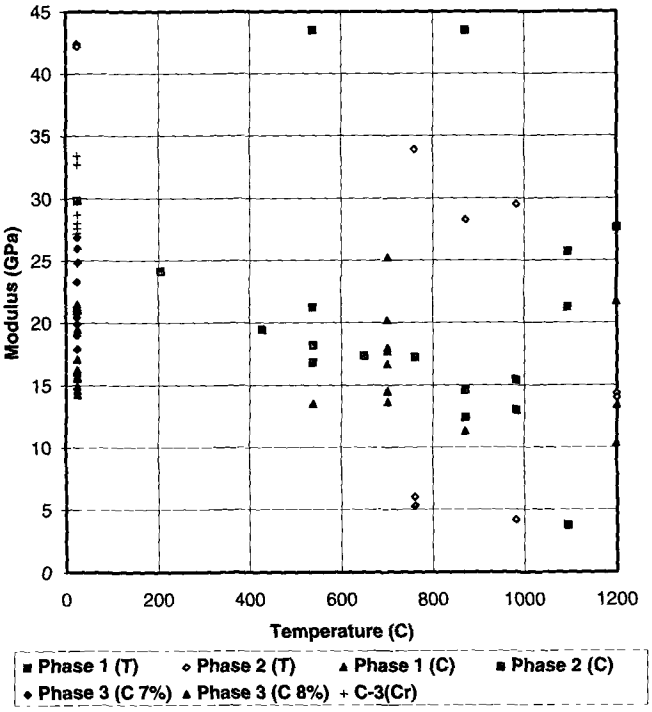

Fig. 5 Modulus data for tests run in tension (T) and compression (C). 7%, 7 wt% yttria PSZ; 8%, 8 wt% yttria PSZ; Cr, cermet

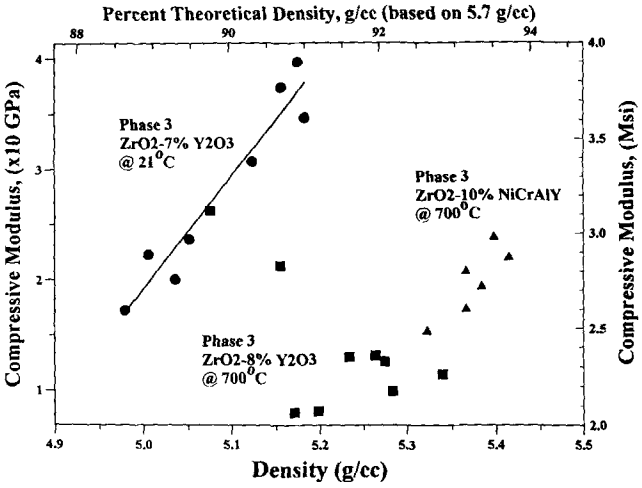

Fig. 6 Compressive modulus vs. material density for two partially stabilized zirconia TBCs and one cermet (PSZ + 10 wt% NiCoCrAlY)

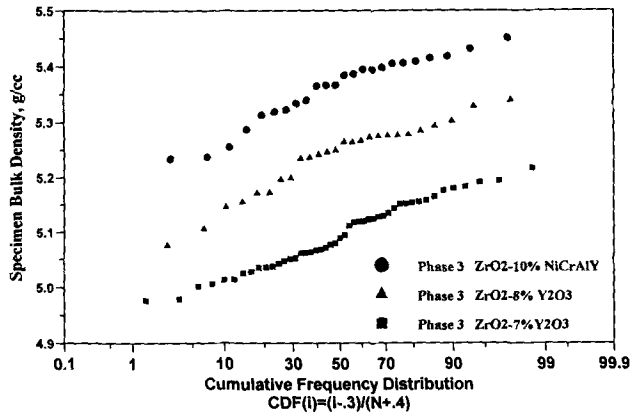

Fig. 7 Cumulative frequency plot of the specimen bulk density data for Phase 3 testing

tween room temperature and 1200 °C, to values that are about half of the room-temperature values.

Figure 6 plots the compressive modulus data with respect to the measured density of the Phase 3 specimens (Ref 7). The cumulative distribution functions of the density data for the three Phase 3 materials are shown in Fig. 7. The scatter in the Phase 3 modulus data shown in the previous figure shows a systematic variation in modulus with density of the 7 wt% yttria PSZ material tested at room temperature. However, the 8 wt% PSZ and the cermet specimens, which have comparable variations in specimen densities, did not exhibit the same systematic variation of modulus with density at room temperature or at 700 °C. Nonetheless, some of the scatter in the modulus data in Fig. 5 may be attributed to variations in specimen density.

The ultimate tensile strength (UTS) data are plotted in Fig. 8. The Phase 1 tensile strength results from Ref 3 are for the wafer and the bowtie specimens. All tensile failures in the bowtie specimen configuration were at the stress concentration at the end of the gage section. Given the difficulty in machining these specimens, the variation in the tensile data is taken to be scatter and not a temperature effect. Creep testing of a single specimen at 538 °C, followed by loading to fracture, resulted in a failure in the gage section at a UTS value of 18 MPa. While no longer notch sensitive, the UTS is consistent with that for the non-creep testing. The average of the bowtie tensile data was 19 MPa. The data are tabulated in Table 2.

The wafer data in Fig. 8 include three static (non-fatigue) data points. The UTS at 538 °C was 23.4 MPa. Two static failures were also obtained at 871 °C, and the strengths were 22.0 and 22.7 MPa. These tensile data suggest that there is no significant temperature difference over that temperature range, an observation consistent with the bowtie data for the same temperatures. While the wafer specimens failed in the center of the specimen transverse to the compressive load, as expected for a tensile failure mode, the stress in the mid-portion of this specimen was biaxial. The average of the three data points, 22.6 MPa, divided by the stress concentration, 1.15, is 19.8 MPa. The data suggest that biaxiality is not an issue but that the stress concentration factor is. Therefore, the tensile strength of the plasma-sprayed PSZ appears to be temperature insensitive over a wide range of temperatures.

Phase 2 composite specimen tension results indicated that the EB-PVD material did have a tensile strength capacity, with fracture of the interfaces between the material columns as the

Table 1 Phase 1 and Phase 2 modulus data by test type (T, C) and test phase (1, 2, 3) in GPa

Temperature, °C	T-1	T-2	C-1	C-2	C-3 (7%)	C-3 (8%)	C-3 (Cr)
24	21.00	42.40	...	29.38	...	21.50	33.40
	...	42.20	...	...	...	17.09	32.70
	...	...	...	...	17.91	15.71	24.80
	...	...	...	...	19.91	14.61	27.60
	...	...	...	...	19.02	16.26	29.80
	...	...	...	...	20.46	16.19	26.00
	...	...	...	...	23.29	15.57	27.20
	...	...	...	...	25.98	19.50	24.80
	...	...	...	...	26.87	14.26	28.70
	...	...	...	...	24.87	14.26	28.00
	...	...	...	...	...	16.05	...
	...	...	...	...	...	14.95	...
204	...	...	...	24.13	...	...	...
427	...	...	...	19.44	...	...	...
538	21.24	...	13.51	16.82	...	...	...
	43.51	...	...	18.19	...	...	...
649	...	...	...	17.37	...	...	...
760	...	33.92	...	17.24	...	...	...
	...	5.31	...	...	...	...	...
700	...	...	...	...	...	20.19	...
	...	...	...	...	...	17.71	...
	...	...	...	...	...	25.22	...
	...	...	...	...	...	17.98	...
	...	...	...	...	...	14.47	...
	...	...	...	...	...	13.64	...
	...	...	...	...	...	14.54	...
	...	...	...	...	...	16.67	...
760	...	6.03	...	...	...	...	...
871	43.51	28.27	11.31	14.62	...	...	...
	12.41	...	12.41	...	...	...	...
982	...	29.51	...	15.43	...	...	...
	...	4.18	...	13.02	...	...	...
1094	21.24	...	...	3.75	...	...	...
	25.72	...	...	...	...	...	...
1200	27.65	14.34	21.72	...	...	...	...
	27.65	14.00	13.44	...	...	...	...
	...	...	10.34	...	...	...	...

T, tension; C, compression; 7%, 7 wt% yttria PSZ; 8%, 8 wt% yttria PSZ; Cr, cermet. Source: Ref 3, 4

tensile fracture mode. Above about 700 °C, the tensile strength value for the EB-PVD material appeared to be on the order of one-half of the strength of the Phase 1 data. The ambient data and some of the higher scatter values suggest tensile strengths approaching 40 to 50 MPa, which would be consistent with the 400 °C tensile strengths reported by Brink (Ref 5). The ambient

Table 2 Phase 1 and Phase 2 ultimate strength data (MPa)

Temperature	Phase 1			Phase 2		Phase 3		
°C	Bowtie (T)	Phase 1 (C)	Wafer (T)	Composite (T)	Phase 2 (C)	Phase 3 (7%)	Phase 3 (8%)	Phase 3 (Cermet)
24	...	...	...	...	...	191.54	...	...
	...	...	...	...	...	241.84	...	...
	...	...	...	...	...	246.66	...	...
	...	...	...	...	...	219.10	...	...
	...	...	...	...	...	242.53	...	...
	...	...	...	...	...	293.51	...	...
	...	...	...	...	...	210.15	...	...
	21.30	...	...	50.50	...	...	...	...
	...	...	...	39.20	...	...	...	...
538	18.30	376.00	23.40	...	...	...	...	...
700	...	...	...	...	...	...	409.13	438.00
	...	...	...	...	...	...	457.77	548.00
	...	...	...	...	...	...	461.63	528.00
	...	...	...	...	...	...	488.78	539.00
760	...	...	...	4.90	455.00	...	...	...
	...	...	...	10.60	481.00	...	...	...
	...	...	...	35.80	...	...	...	...
871	17.80	303.00	22.00	...	...	...	...	...
	18.50	274.00	22.70	26.20	...	...	...	...
982	...	...	...	18.00	446.00	...	...	...
	...	...	...	4.00	428.00	...	...	...
1094	21.30	...	...	...	...	...	...	...
	21.90	...	...	9.40	...	...	...	...
1204	16.90	198.00	...	6.90	...	...	...	...
	16.00	218.00	...	7.40	...	...	...	...
	...	273.00	...	...	...	...	...	...
Averages:	19.00	273.80	22.70	19.35	452.50	235.05	454.33	513.25

T, tension; C, compression; 7%, 7 wt% yttria PSZ; 8%, 8 wt% yttria PSZ. Source: Ref 3, 4

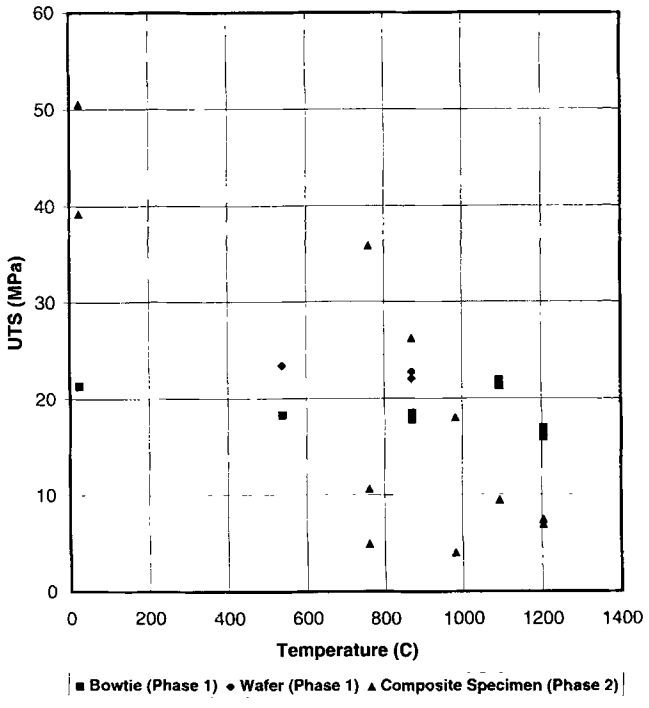

Fig. 8 Ultimate tensile strength vs. temperature for the bowtie, wafer, and composite specimens

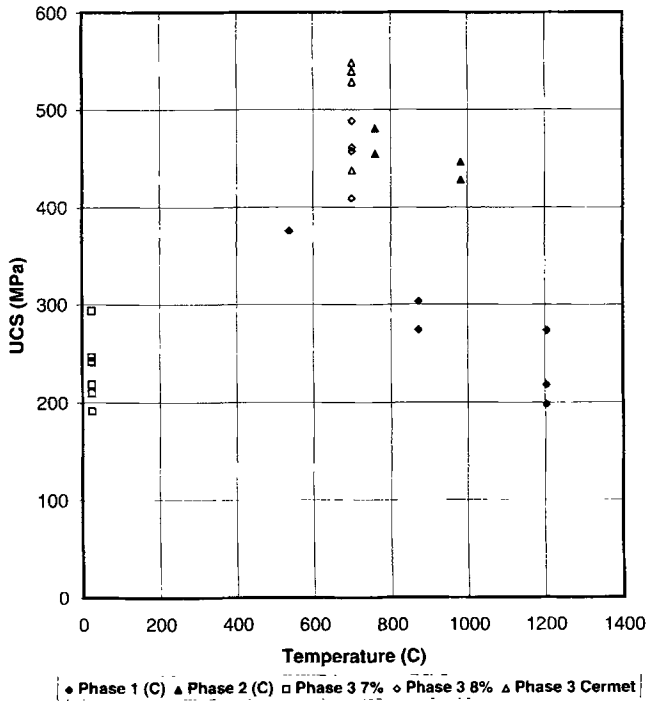

Fig. 9 Ultimate compression strength vs. temperature. C, compression; 7%, 7 wt% yttria PSZ; 8%, 8 wt% yttria PSZ

temperature values of the tensile strength were strongly dependent on the computed modulus of the material; residual stresses in the TBC were indicated in the tests that affect the modulus calculations. We therefore discount the Phase 2 values of the tensile strength of the TBC at ambient temperature. There are no Phase 3 tensile data.

Few, if any, of the specimens showed linear tensile stress-strain behavior. The Phase 2 tensile data was especially vulnerable to errors in the assumed linear behavior and the derived modulus. Further, the role of the substrate was critical, as was the role of bending strains. The fracture of a simple bowtie specimen of TBC was quite unlike that of the TBC when it was supported on a metal substrate, as in the Phase 2 testing. In terms of component design, the benefits of support are likely to give a higher effective tensile strength as well as the possibility of beneficial residual stresses away from the ends of the TBC.

The compressive strength data are shown in Fig. 9. The Phase 1 cylinder data suggest that the compressive strength showed a stronger temperature effect than that for the tensile data, although no ambient testing was performed. The Phase 2 composite specimen and the 8 wt% yttria PSZ materials used in Phase 3 have higher compressive strengths than the Phase 1 specimen and the 7 wt% yttria PSZ used in Phase 2. The compressive strengths of the Phase 3 cermet material (PSZ + 10 wt% Ni-CoCrAlY) appear to be about 13% higher than those of the 8 wt% yttria PSZ material.

The 7 wt% yttria PSZ used in Phase 3 can be discounted, because the specimens exhibited "mudflat" cracks. The cracks were widely distributed on the surface and were probably due to swelling of the interface between the ceramic and the substrate during acid etch removal of the substrate. The compressive failure origins appeared to be at 45° to the load axis and originated at mudflat cracks, indicating their role in promoting a surface shear fracture. The Brink data (Ref 5), obtained using a composite bend specimen, indicated that PSZ and cermet strengths were in excess of 500 MPa at 400 °C, indicating a possible trend to higher strengths at lower temperatures than the data reported herein. More recently, Jesling et al. (Ref 8) have given data for 8 wt% yttria PSZ, showing compressive strengths of 450 MPa at 805 °C and 520 MPa at room temperature. These data appear most comparable to ours and strongly suggest a lack of temperature influence on compressive strength over this lower temperature range.

Figure 10 plots the Phase 3 compressive strength data for the three materials in terms of the specimen density. In this case, all three data sets show a consistent trend of strength with density. These specimens appear to have failed in an axial splitting mode. Limited scanning electron microscopy of the failure surfaces in the 8 wt% yttria PSZ and cermet specimens indicated that the failures cannot be associated with any material or structural abnormality. The investigation concluded that the intrinsic structure of the plasma-sprayed materials is the likely source of the specimen fractures in the absence of mudflat cracks.

Given the density trend similarities in the compressive strength data and the differences in the nature of the failure origins, we conclude that flaw sensitivity of the plasma-sprayed TBCs in all three test programs depended on material density. However, because material density and flaw sites are complementary (the flaws primarily being voids between splats), the trend would likely relate to a decrease in the statistical flaw size of the TBC with increasing material density. This would also explain the much lower strengths of the specimens with mudflat cracks, in that the mudflat cracks act as stress risers on the intrinsic material defects.

4. Fatigue Results

Phase 1 and Phase 2 testing focused on thermomechanical fatigue for gas turbine applications. This testing has been reported in Ref 3 and 4. Phase 3 testing focused on compressive stress isothermal fatigue for diesel cycle engines.

Limited tensile fatigue testing of the 7 wt% yttria PSZ was performed using the wafer test, as reported in Ref 3. The testing was done at $R = 0.1$, at stress levels that were about 90% of the tensile strength of the specimens. The fatigue lives of the specimens were only hundreds of cycles, as plotted in Fig. 11, but a specimen runout was obtained at slightly less stress amplitude. Table 3 gives the fatigue data.

Table 3 Phase 1 fatigue test results (alternating stress in MPa)

	Phase 1	Phase 2				
Cycles	Wafer	7%	8%	Cermet	400 °C (8%)	Ref 10
195	16.5	...	...	...	...	...
307	16.5	...	...	...	...	...
410	16.5	...	...	...	...	...
158	16.4	...	...	...	...	...
407	16.4	...	...	...	...	...
2,400	...	–202.8	...	...	...	...
25,460	...	...	–160	...	...	...
90,930	...	...	–160	...	...	...
540,900	...	...	–160	...	...	...
707,925	...	...	–160	...	...	...
733,810	...	...	...	–185	...	...
20,740	...	...	...	–185	...	...
21,020	...	...	...	–185	...	...
105,400	...	...	...	–185	...	...
15,000	...	...	...	...	...	–225
300,000	...	...	...	...	...	–190
20,000,000	...	...	...	...	–152	...

7%, 7 wt% yttria PSZ; 8%, 8 wt% yttria PSZ. Source: Ref 3

Compressive fatigue testing was done on the Phase 3 program for all three materials. The 7 wt% yttria PSZ material was tested at several stress levels at 700 °C. A number of runouts occurred at lower initial cyclic stresses, but there was one successful fatigue failure at a cyclic stress range of 203 MPa with a life of 2400 cycles. Based on the compressive strength testing results for that material, the cyclic stress range was about 86% of the material compressive strength.

The 8 wt% yttria PSZ material was initially tested in fatigue at 700 °C with no failures to a runout of 2×10^6 cycles and at cyclic stresses on the order of 50% ($R = 0.6$). The maximum compressive stress was selected to be about 90% of the compressive strength of the materials. The same cyclic stress conditions were then applied at room temperature, and fatigue lives were in the expected range for both the 8 wt% yttria PSZ and the cermet materials. Figure 11 shows the cyclic stress amplitude applied to the various fatigue specimens from Phase 1 and Phase 3 testing, as well as two test points from Ref 10. One runout test point (21 million cycles) for the 8 wt% yttria PSZ is also shown; the test temperature was 400 °C.

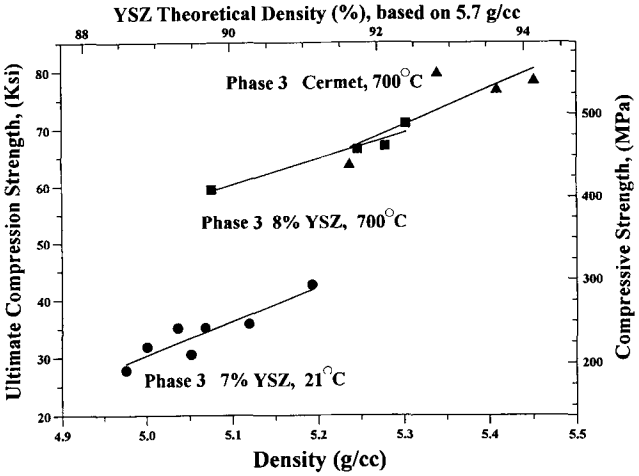

Fig. 10 Ultimate compression strength vs. material density for 7 and 8 wt% yttria partially stabilized zirconia (YSZ) and one cermet (PSZ + 10 wt% NiCoCrAlY)

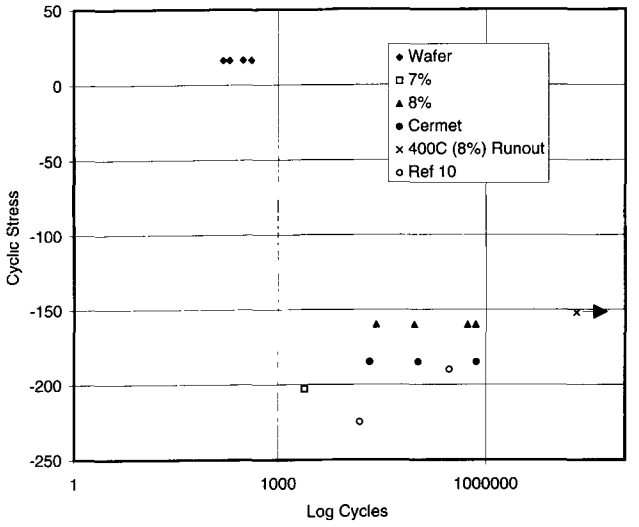

Fig. 11 Room-temperature fatigue testing results in tension and compression with runout at elevated temperature. 7%, 7 wt% yttria PSZ; 8%, 8 wt% yttria PSZ

The current test program and that reported in Ref 10 were performed on comparable materials, all prepared by Caterpillar Inc. However, the referenced work was for $R = 0.1$, while the current one was for $R = 0.6$. Figure 11 shows that the two very different mean stress conditions produced quite comparable fatigue lives. The maximum cyclic stress in the current data is about 90% of the material compressive ultimate, while that from Ref 10 is about one-half the material ultimate. We therefore conclude that the high-cycle fatigue damage process is independent of the maximum cyclic stress, and thus also independent of the mean cyclic stress.

The compressive fatigue failure mechanism appears to behave like a tensile fracture mechanics crack growth mode. It has been found that cyclic crack growth under tensile stresses is independent of the stress ratio; rather it depends solely on the cyclic stress magnitude (Ref 11). This suggests that the compressive fatigue mechanism is one of subcritical crack growth in the TBC materials from the intrinsic defect structures in plasma-sprayed systems.

The transverse stresses on the intrinsic defects in the plasma-sprayed materials (Phase 1 and Phase 3) are tensile for applied compressive axial stresses. The same stress mechanism seems to be the failure mechanism at compressive ultimate load conditions. Figure 12 shows the fatigue lives of the 8 wt% yttria PSZ and the cermet materials from Phase 3, plotted against the measured specimen material densities. The data suggest a positive correlation of fatigue life with increasing density (at least for the Phase 3 PSZ material), which corresponds to a statistically decreasing population of intrinsic defects.

The design implications of this are important at the lower operating temperatures (apparently below 700 °C). The fatigue failure behavior found on two of the many test specimens that were generated for the Brink paper (Ref 5) included two spallation failures, one of which is shown in that reference. The spallation failure was seen to be quite like the spallation failure of a TBC in an engine test at Caterpillar. On flat surfaces, the transverse fracture mechanics mechanism that is now postulated

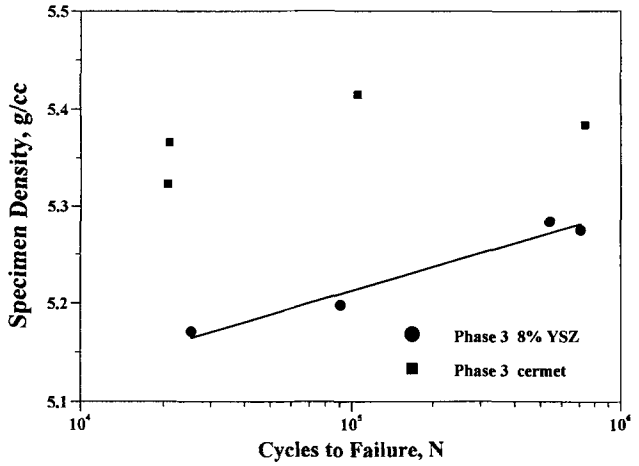

Fig. 12 Cross plot of fatigue specimen density with cycles to failure

would lead to the type of spallation event seen in the Brink paper.

The design goal is to keep the cyclic stresses below about 150 MPa compressive for operating conditions below 700 °C. However, Ref 10 and this paper show that the behavior of these materials above 700 °C suggests an active strengthening mechanism that effectively raises the fatigue limit for the material. Although the mechanisms are not yet fully resolved, the next section discusses the cyclic strengthening process.

5. Cyclic Stress-Strain Results

The original high-temperature work in Phase 1 found that there was significant creep behavior of the TBC material at and above 871 °C (Ref 3). The data were measured using the same tensile and compressive specimens used for modulus and strength data. The tests were run under static applied stress conditions, and the steady creep strain rate was taken experimentally. Creep tests could not be performed in the Phase 2 tests.

The Phase 3 fatigue test program found that the specimens were significantly shorter at the suspension of fatigue testing. The length reductions were on the order of 0.5 to 1.0 mm and were found for tests run at room temperature as well as at elevated temperatures. These length reductions were subsequently found to be associated with a transient process of cyclic ratchetting of the compressive strains. The ratchetting might be likened to a "stick-slip" type of process.

Figure 13 shows representative data for head displacement versus test time for three of the fatigue specimens previously reported. There were two tests at room temperature (specimens 5-2 and 3-3). These fatigue tests were at the same maximum (400 MPa) and cyclic (160 MPa) stresses. The first failed at about 708,000 cycles and the second at about 91,000 cycles. Also plotted are data for a runout test at 400 °C with a maximum stress of 379 MPa and a cyclic stress of 152 MPa. The room-temperature tests were run at 25 Hz, while the elevated-temperature test was run at 60 Hz.

There does not appear to be a correlation between these test conditions and the cyclic ratchetting process. It seems that the mechanism of the ratchetting is independent of the failure mechanism, the stress level, and the cyclic frequency. In order to better define the cyclic ratchetting phenomenon, several "four-cycle" tests were performed in Phase 3.

Four-cycle data were obtained by loading each specimen to successively higher loads. A constant preload of about 450 N was maintained on the specimens for all four load cycles. The additional loading was applied at a constant stroke rate over an interval of 20 to 30 s; the entire four-cycle loading took about 3 min. Specimen length was measured prior to and after the tests on five of the eight specimens. Modulus data were recorded for each load cycle and are shown for the first and last of the cycles in Table 4.

The four-cycle modulus data show that the cyclic response of the material causes the specimen length to be reduced, and they also show that significant changes occur in the measured specimen moduli. The same basic phenomenon was also cited in Ref 10. Compressive strength testing of the specimens after fatigue testing, during which this cyclic ratchetting was occurring, shows that the compressive fracture strength is significantly elevated as well as the material modulus.

The fatigue test data suggest that the cyclic hardening process occurs at temperatures above 400 °C at a high enough rate that the fatigue cracking process is greatly forestalled, if not eliminated. Very limited fatigue testing at increasing levels of applied stress has shown that stresses much higher than the original material strength fail to cause fatigue failures in very high numbers of total cycles. The phenomenon was observed in one Phase 1 wafer test as well as in several Phase 3 tests of 7 and 8 wt% yttria PSZ.

Such cyclic hardening and the known creep behavior of the material at high temperatures clearly show that a more advanced material constitutive model is required in order to make realistic life predictions under cyclic stress conditions over a range of temperatures.

6. Conclusions

Mechanical test data from several different phases of experimental work with ceramic coatings have been reported. Investigations of the compressive modulus and strength of the ceramic specimens resulted in reasonably consistent results. Material density and cycling influenced these properties. Compressive failure was most likely caused by the splitting of intrinsic defects in the material, for both static loading and fatigue loading. The fatigue damage process was likely one of subcritical crack extension from these intrinsic defects and was somewhat mitigated by higher material density.

Tensile testing data contained much more scatter than data for the compressive tests. The tensile behavior of TBCs was generally nonlinear, probably due to the creation and extension of multiple microcracks in the material. As expected, the material was notch sensitive over a wide range of temperatures, but it be-

Table 4 Four-cycle modulus data

Material	Specimen ID	ΔL, mm	Density, cm^3	1st cycle E, GPa	4th cycle E, GPa	Modulus change, GPa
8 wt% yttria	1-3	Not measured	5.171	14.2	24.4	10.2
	3-3	Not measured	5.198	14.3	24.0	9.7
	5-2	0.051	5.275	16.0	28.7	12.7
	7-4	0.038	5.284	15.0	24.9	9.9
Cermet	15-2	Not measured	5.384	18.7	28.6	9.9
	15-4	0.064	5.323	17.1	25.7	8.6
	18-1	0.051	5.415	19.8	28.1	8.4
	11-1b	0.051	5.366	19.3	29.5	10.2

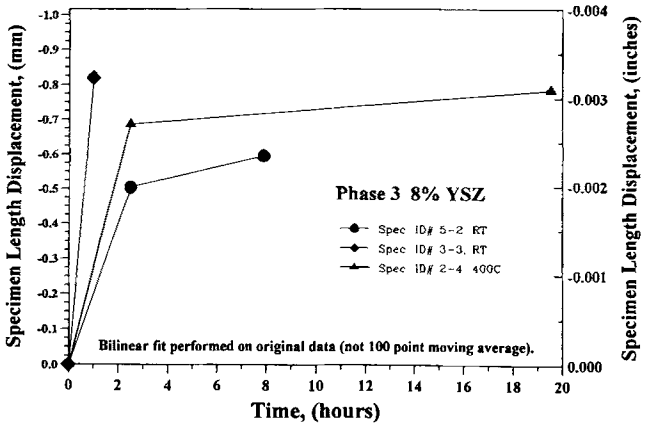

Fig. 13 Representative data, selected from previously reported results, for specimen length change vs. test time

came notch insensitive in the creep regime. Tensile fractures are likely to be caused by the same defect structures in the ceramics as those for the compressive stress, but are obviously triggered at much lower levels of applied stress.

The material was found to have very complex cyclic behavior at all temperature ranges. The use of elastic stress analysis models for design work is not likely to be appropriate due to the cyclic ratchetting and creep process effects on the stress state of the material through a redistribution of the material strains. More work is needed to properly model the behavior of these materials in engine operating conditions.

Acknowledgments

We gratefully acknowledge the significant support given to this effort by Dr. Robert A. Miller of the NASA Lewis Research Center; by J.T. DeMasi, K. Sheffler, S.M. Meier, M. Ortiz, and D.M. Nissley of Pratt & Whitney Aircraft; and by B. Beardsley of Caterpillar, Inc. The work was financially supported through a series of cooperative agreements with NASA Lewis Research Center and Pratt & Whitney. The Phase 1 and Phase 2 tests were performed for Pratt & Whitney under NASA sponsorship, while Phase 3 testing was performed directly for NASA. The mechanical tests were developed under the direction of the principal author, Phase 1 and Phase 2 testing was performed by Mr. Nagy, and Phase 3 testing was performed by Mr. Johnsen.

References

1. T.A. Cruse, S.E. Stewart, and M. Ortiz, Thermal Barrier Coating Life Prediction Model Development, *J. Eng. Gas Turbines Power*, Vol 110, 1988, p 610-616
2. S.M. Meier, D.M. Nissley, K.D. Sheffler, and T.A. Cruse, Thermal Barrier Coating Life Prediction Model Development, *J. Eng. Gas Turbines Power*, Vol 114, 1992, p 258-263
3. J.T. DeMasi, K.D. Sheffler, and M. Ortiz, "Thermal Barrier Coating Life Prediction Model Development, Phase I—Final Report," NASA Contractor Report 182230, 1989
4. S.M. Meier, D.M. Nissley, and K.D. Sheffler, "Thermal Barrier Coating Life Prediction Model Development, Phase II—Final Report," NASA Contractor Report 189111, 1991
5. R.C. Brink, Material Property Evaluation of Thick Thermal Barrier Coating Systems, Paper 89-ICE-13 , *Proc. 1989 Energy Sources Technology Conf.*, American Society of Mechanical Engineers, 1989
6. T.A. Cruse, B.P. Johnsen, R.A. Miller, and W.J. Brindley, Compressive Fatigue Behavior of a PSZ TBC—Status Report, *Proc. 1992 Coatings for Advanced Heat Engines Workshop* (Monterey, CA), Office of Transportation Technologies, U.S. Dept. of Energy, Washington, D.C., 1992, p II-41 to II-47
7. B.P. Johnsen, T.A. Cruse, R.A. Miller, and W.J. Brindley, Compressive Fatigue of a Plasma Sprayed ZrO_2-8%wtY_2O_3 and ZrO_2-10%wtNi-CoCrAlY TTBC, *J. Eng. Mater. Technol.*, Vol 117 (No. 3), 1995, p 305-310
8. M.C. Shaw, P.M. Braiden, and G.J. DeSalvo, The Disk Test for Brittle Specimens, *J. Eng. Ind.*, Vol 97, 1975, p 77-87
9. T.A. Cruse, A. Nagy, and C.F. Popelar, "Mechanical Testing of Advanced Coating System," Final Report, NASA Cooperative Agreement NCC3-89, Southwest Research Institute, San Antonio, TX, 1990
10. K.F. Wesling, D.F. Socie, and B. Beardsley, Fatigue of Thick Thermal Barrier Coatings, *J. Am. Ceram. Soc.*, Vol 77 (No. 7), 1994, p 1863-1868
11. D. Broek, *Elementary Engineering Fracture Mechanics*, Martinus Nijhoff, Amsterdam, 1986